Journal of Materials Science & Technology 233 (2025) 255–263

Contents lists available at ScienceDirect

Journal of Materials Science & Technology

journal homepage: www.elsevier.com/locate/jmst

Research Article

Giant charge trapping in 2D layered oxide nanosheets via intrinsic quantum wells

Kyungjune Cho[a,b,1,*], Haena Yim[c,1], Gahui Park[a], Jiwoo Yang[a], So-Yeon Yoo[c], Jongwoo Nam[d], Minwoo Song[d], Deok-Hwang Kwon[e], Keehoon Kang[f], Takhee Lee[d], Ji-Won Choi[c,g,*], Seungjun Chung[h,*]

[a] *Soft Hybrid Materials Research Center, Korea Institute of Science and Technology, Seoul 02792, Republic of Korea*
[b] *Convergence Research Center for Solutions to Electromagnetic Interference in Future-mobility, Korea Institute of Science and Technology, Seoul 02792, Republic of Korea*
[c] *Electronic Materials Research Center, Korea Institute of Science and Technology, Seoul 02792, Republic of Korea*
[d] *Department of Physics and Astronomy, and Institute of Applied Physics, Seoul National University, Seoul 08826, Republic of Korea*
[e] *Center for Energy Materials Research, Korea Institute of Science and Technology, Seoul 02792, Republic of Korea*
[f] *Department of Materials Science and Engineering, Research Institute of Advanced Materials, Seoul National University, Seoul 08826, Republic of Korea*
[g] *Nanoscience and Technology, KIST-School, Korea University of Science and Technology, Seoul 02792, Republic of Korea*
[h] *School of Electrical Engineering, Korea University, Seoul 02841, Republic of Korea*

ARTICLE INFO

Article history:
Received 22 November 2024
Revised 15 January 2025
Accepted 15 January 2025
Available online 17 March 2025

Keywords:
Two-dimensional material
Charge trapping
Intrinsic quantum well
Persistent photoconductivity
Oxide perovskite

ABSTRACT

The atomically thin nature of two-dimensional (2D) layered materials makes them susceptible to charge trapping by randomly created disorders, adversely affecting carrier dynamics such as charge transport and exciton lifetime. Typically, these disorders lead to poor device performance or require additional space to mitigate performance degradation. In this study, we investigate 2D layered Dion–Jacobson (DJ)-phase oxide perovskite nanosheets, which exhibit charge trapping within their well-defined quantum well (QW) structures, resulting in unique tailoring of electrical conductivity and photoconductivity. These DJ-phase perovskites, composed of tunable atomic constituents, demonstrate resonant tunneling and anomalous charge trapping due to their ultra-clean QWs. Remarkably, the conductivity of insulating $HSr_2Nb_3O_{10}$ (HSNO) increased over 1000 times upon applying voltage without additional treatments. We observed persistent photoconductivity in 2D vertical heterostructure devices, attributed to charge trapping in QWs, and demonstrated artificial synaptic behaviours in a single flake with tailored energy consumption. Varying the number of perovskite layers significantly allows the tunability of the energy bandgap. This study also highlights the high tunability of 2D perovskite nanosheets, promising various applications, including magnetic, high-k dielectric, and resistive switching devices. Our findings suggest a new class of ionic layered materials with great potential as novel two-dimensional building blocks for device applications.

1. Introduction

Two-dimensional (2D) layered materials are one of the most promising candidates for advanced semiconductor technologies owing to their diversity and superior properties, which have led the discovery of various 2D layered material families [1–8]. However, their atomically thin nature make injected or generated charges susceptible to trapping by randomly created disorders, which can significantly affect carrier dynamics such as charge transport or exciton life time [5,9–15]. These disorders in 2D materials can hinder charge transport, leading to poor device performance, or require additional space to avoid unwanted performance degradation. Although charge trapping layers with a high concentration of disorders, has been introduced in memory device applications [5,9,16–27], it is still challengable to control their performance elaborately due to the unexpectable trapping behaviour in structurally random disorders. Therefore, a new class of 2D layered materials which have well-defined charge trapping layers with a high degree of design freedom are necessary to tailor the electrical and optical characteristics of 2D layered materials, especially in a sinlge flake or vertically stacked heterostructures where current flows through the charge trapping layers.

---

* Corresponding authors.
E-mail addresses: kcho@kist.re.kr (K. Cho), jwchoi@kist.re.kr (J.-W. Choi), seungjun@korea.ac.kr (S. Chung).

[1] These authors contributed equally to this work.

https://doi.org/10.1016/j.jmst.2025.01.042
1005-0302/

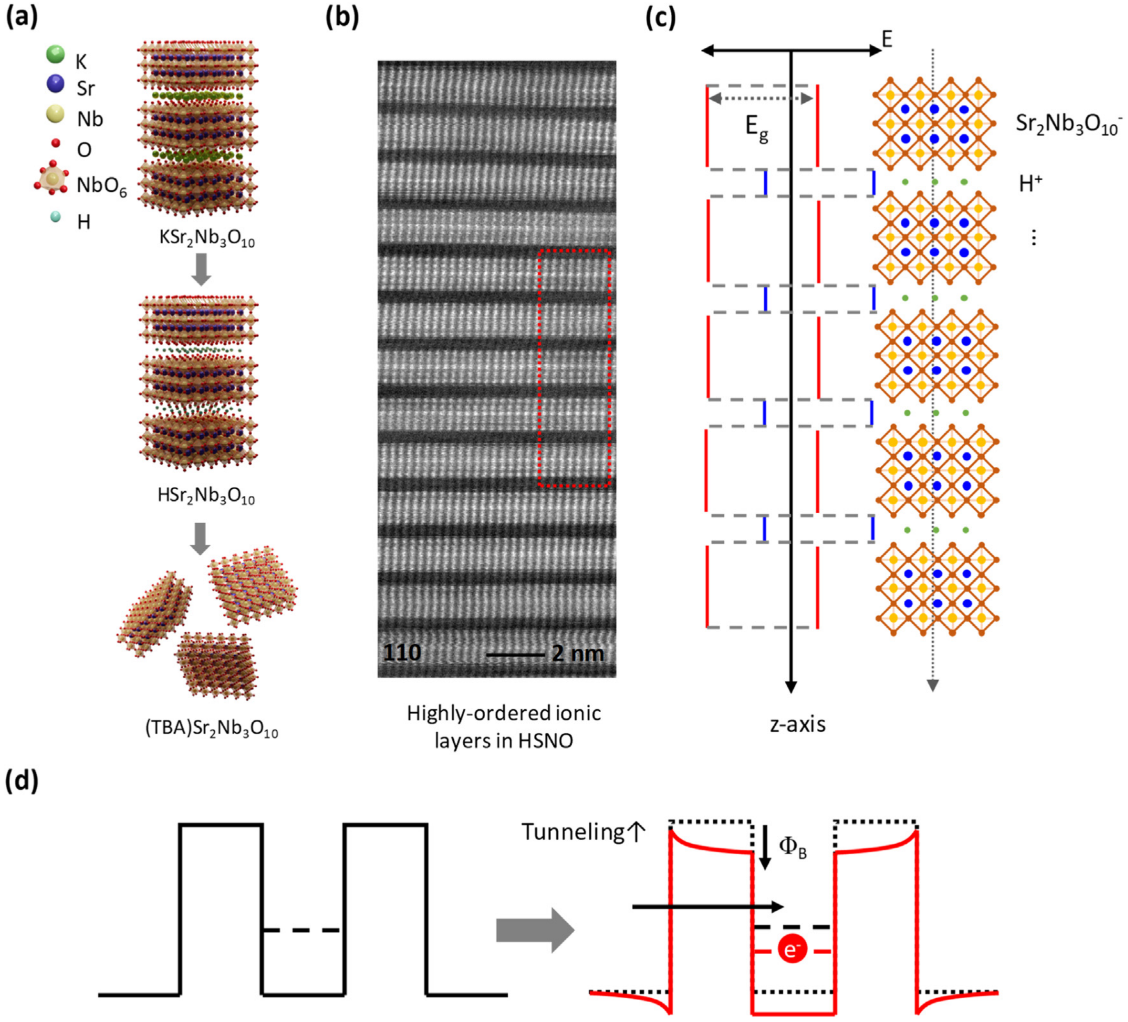

Fig. 1. (a) Schematic illustrations of the material synthesis process. (b) STEM image of the intrinsic highly-ordered ionic layers in HSNO and (c) the energy band diagram along the z-axis. (d) Schematic energy structure before and after charge trapping in a QW.

In this study, we discovered 2D layered Dion–Jacobson (DJ)-phase oxide perovskite nanosheets, specifically $HSr_2Nb_3O_{10}$ (HSNO), exhibit unique charge trapping in their intrinsic and well-defined quantum well (QW) structures resulting in giant enhancement in electric and photoconductivity. DJ-phase perovskites are composed of four different atomic constituents which provides high tunability: $A'A_{n-1}B_nX_{3n+1}$, where A'^{+} is a positively charged cation and $[A_{n-1}B_nX_{3n+1}]^-$ is the anion part. Unlike those of typical 2D vdW layered materials, the thinning of these oxide perovskite materials is difficult because of the strong ionic bonding between layers. However, recent advancements have shown that exchanging small cations in DJ-phase perovskites with larger cations, such as tetrabutylammonium (TBA), can promote the exfoliation of layered oxide perovskites down to the monolayer limit [28–32].

In the case of $HSr_2Nb_3O_{10}$ (HSNO) we used in this study, the structure is composed of positively charged proton layers (H^+) and negatively charged $Sr_2Nb_3O_{10}^-$ (SNO) layers in HSNO flakes, as depicted in Fig. 1(a) and as shown in the scanning transmission electron microscopy (STEM) image (Fig. 1(b) and S2 in the Supplementary materials). We found that alternatively stacked cation and anion layers can form the well-defined ionic and layered structures along the z-axis and corresponding QW structures owing to their Coulomb potential as illustrated in Fig. 1(c). In addition, we discovered that the compatibility of 2D layered HSNO with the conventional vdW transfer method which can offer tremendous possibilities to provide the designed functionalities of emerging 2D devices, freeing up their material combinations as needed. By utilizing this compatibility, we were able to fabricate transparent vertical junction devices with sandwiched HSNO flakes and graphene (Gr) top and bottom electrodes. This device structure allows us to explore the native quantum mechanical properties of intrinsic highly-ordered ionic layered HSNO due to their passive nature (More details are described in the Supplementary materials).

As a result, resonant tunneling through the native QWs and anomalous huge charge trapping in the energy barrier structures were observed owing to the well-defined QWs with intrinsically ultra-clean interfaces, even in a single nanosheet without complicated artificial superlattice or heterostructure fabrication processes. Remarkably, the conductivity of insulating HSNO increased by more than 1000 times upon applying voltage due to giant charge trapping in QWs, without any additional functional layers or treatments. In addition, we observed for the first time the persistent photoconductivity (PPC) in the vertical heterostructure devices which is attributed to the charge trapping in QWs, while 2D materials exhibited ultrafast photoresponse in the vertical structure. By exploiting these tenable changes in conductivity derived from native QWs and their charge trapping properties (Fig. 1(d)), we demonstrated artificial synaptic devices as a potential application. In particular, we successfully tailored the energy consumption of spikes for modulating conductivity by controlling the tunneling probability through the energy barrier of QWs. Furthermore, we showed the high tunability of 2D perovskite nanosheets that promises various classes of additional emerging applications, such as magnetic, high-k dielectric, and resistive switching devices by changing the ions and using substitutional doping. Additionally, by varying the number of perovskite layers, we effectively altered the thickness of each anion layer, i.e., the QW spacing. These were found to influence the tunability of the energy bandgap significantly.

2. Results and discussion

2.1. Controlled liquid phase exfoliation of ionic layered structures

To obtain the HSNO flakes with target thickness, bulk $KSr_2Nb_3O_{10}$ (KSNO) crystals were firstly prepared *via* solid-state synthesis. Potassium ions in KSNO were exchanged with H^+ ions, which were sequentially changed to TBA^+ ions using an ion-exchange method. During this process, the crystal size and thickness decreased as shown in the SEM images (Fig. 2(a and b)), and liquid-phase exfoliation was promoted owing to the large size of TBA^+ ions resulting in monolayer SNO flakes ultimately. The thickness of HSNO was scalable depending on the time of the ion-exchange process from H^+ to TBA^+ and the centrifugation process. The exfoliated monolayer TBA-SNO flakes exhibit good quality including high crystallinity (Figs. S3 and S4), as shown in the TEM image (Fig. 2(c)) and selected area electron diffraction (SAED) pattern (Fig. 2(d)). In this study, we intentionally tuned the TBA^+ ion-exchange time to produce few-layer HSNO flakes in which intrinsic ionic layered structures are created (More details are described in the Supplementary materials). By reducing the ion exchange time and centrifugal speed, we could avoid further exfoliation and achieve thicker nanosheets. The Langmuir–Blodgett (LB) deposition method was employed to transfer HSNO flakes and TBA-SNO flakes onto the target $SiO_2/p{+}{+}$ Si substrate as shown in Fig. 2(e). The residual TBA^+ ions were eliminated with the UVO surface treatments, and the monolayer SNO flakes and multi-layered HSNO flakes were then left as indicated in the optical microscope (OM) image in Fig. 2(e). Additionally, the dimensions of the exfoliated HSNO flakes can be readily adjusted, ranging from a few micrometers to several tens of micrometers, by fine-tuning the synthesis and exfoliation conditions (More details are described in the Supplementary materials). The thickness of the transferred flakes was also measured (Fig. S5). For example, the selected flake shown in Fig. 2(f) has three layers with a thickness of ~6.1 nm, as deduced from the atomic force microscopy (AFM) measurements; this result is consistent with those of previous reports [31]. Only the multilayer HSNO flakes were used to investigate the behavior of ionic layered structures because there is no ionic layered structure in a monolayer SNO flake. The SNO flake has an estimated energy bandgap of 3.9 eV extracted from the UV absorption spectrum, and the UV absorbance increased with higher numbers of LB depositions, as shown in Fig. 2(g). The STEM image reveals the layered structure of negatively charged SNO flakes with a gap, where the protons between neighboring SNO layers satisfied charge neutrality, indicating the intrinsic ionic layered structure (Fig. 2(h) and S2). Notably, the TBA^+ moiety is much larger than the observed gap for the protons [33].

We further verified the creation of the ionic layered structures by measuring the electrical characteristics of hexagonal boron nitride (*h*-BN)/Gr/HSNO/Gr vertical junction heterostructure devices (Fig. 2(i) and S19). The HSNO flakes can be picked up using the conventional vdW transfer method with polypropylene-carbonate-coated PDMS stamps (Figs. S16 and S17). Specifically, passive Gr electrodes were introduced to investigate the intrinsic properties of the HSNO layers, which enables repeated observation of the clear resonant tunneling behavior in several devices even at room temperature owing to the atomically clean interfaces of intrinsic layered structures (Figs. 2(j) and S22). We could not observe resonant tunneling using conventional metal electrodes, such as silver (Ag) and gold (Au), because not only their rough surface but also the diffusion of metal ions into the HSNO layers occurs, resulting in poor interfacial properties and causing the intermixing of different effects to charge transport (Supplementary materials Section 5). The resonant tunneling, along with the corresponding negative differential resistance, is unique to intrinsic QW structures, which can be induced by the Coulomb potential from ionic layers [1,34–36]. We observed shifts in resonant tunneling voltage when the thickness of SNO varied, which is likely due to changes in the electric field (Fig. S22).

2.2. QW-driven unprecedented PPC and charging effect

In addition to resonant tunneling, we observed unprecedented PPC after UV illumination, especially in the vertical junction devices as shown in Fig. 3(a). PPC has been known to be introduced by the random potential fluctuation in the energy band due to defects that trap charges from excitons, creating the gate-like electric field which increases the conductivity of the channe [9–14,37]. This photogate effect has been often observed in 2D semiconducting systems which have high-defect densities, such as lateral MoS_2 field-effect transistors (summarized in Table S2). Note that we conducted all characterizations in an inert environment to investigate their intrinsic properties and to avoid unwanted trap-mediated recombination effects from the environment that can suppress PPC. To the best of our knowledge, it has never been observed in a 2D vertical junction device due to the high electric field across the vertical junction and consequential tunneling transport nature. This tunneling phenomenon under a high electric field makes trapping of injected and photogenerated charges difficult in a vertical junction because such trap sites would be shallow from an energy perspective. Thus, even if charges were trapped, they would be de-trapped after a short time. In this frame, vertical junction devices rather exhibit ultrafast charge recombination because the generated excitons would be separated and rapidly escape to the top and bottom electrodes [37–39]. However, surprisingly, we observed an unprecedented ultra-long PPC behavior in our ionic layered structure with the vertical junction structure, as shown in Fig. 3(a). This PPC can be attributed to the QWs in the HSNO flake with naturally created superior interfaces forming intrinsic Coulomb potential barriers (Fig. 3(b)). According to previous studies, these QWs can trap photogenerated charges that can induce a gate-like electric field, increasing the conductivity, i.e., the photogate effect [40,41]. Upon charge entrapment within the quantum wells, the associated electric fields from these trapped charges reduce the energy barriers, consequently enhancing the conductivity of the channel (More details are described in the Supplementary materials Section 7). It should be noted that investigating the relationship between photocurrent and light power density to determine whether photoconduction or photogating is dominant was challenging. This is due to the continuous increase in photocurrent over time and the high bandgap of SNO. Additionally, limitations in accessing a power-adjustable UV laser further hindered our ability to evaluate the relationship between photocurrent and light power density effectively. In particular, the current across the vertical junction increased exponentially with increasing voltage bias, which also supported the vertical tunneling through the QWs at the junction. Under such circumstances, the conductivity enhancement under

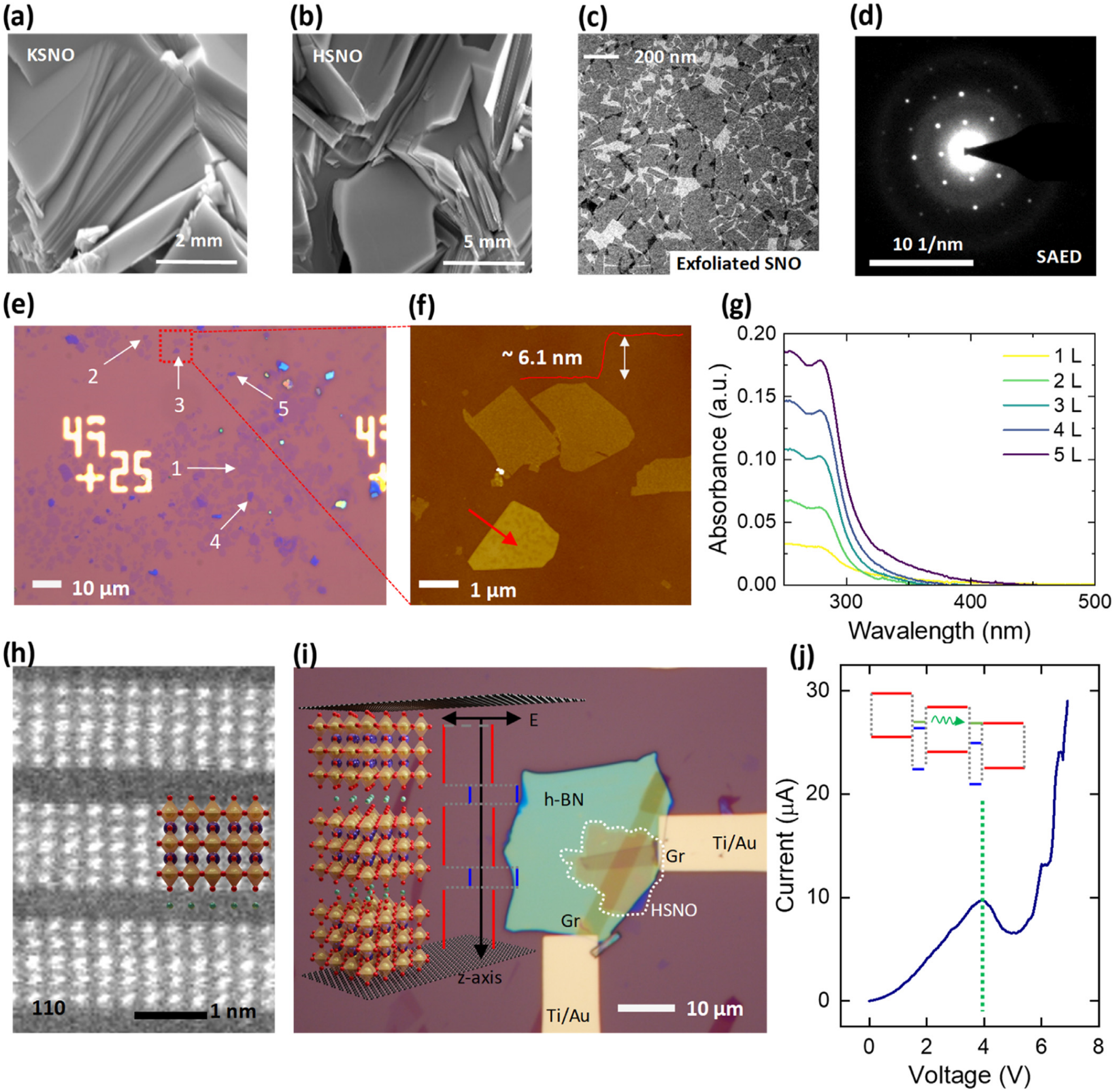

Fig. 2. SEM images of the (a) KSNO and (b) HSNO flakes. (c) TEM image of the SNO flakes and (d) their SAED image. (e) Optical image of the transferred HSNO and SNO flakes on the $SiO_2/p{+}{+}$ Si substrate. Written numbers indicate the number of layers of each flake. (f) AFM image of a selected area. The flake indicated with a red arrow is the same flake as the tri-layer HSNO flake in (e). (g) UV absorption spectrum of the SNO flakes. The numbers in the legend indicate the number of the LB deposition. (h) STEM image of the highly-ordered ionic layered structure in HSNO. (i) Optical image of a vertical junction *h*-BN/Gr/HSNO/Gr heterostructure device. Schematics depict the vertical junction device structure and its energy band diagram along the z-axis. (j) Current versus voltage curve showing a resonant tunneling behaviour.

UV illumination would be faster at a higher voltage regime because the generated charges need to tunnel through the QWs and the tunneling probability exponentially increases with increasing applied voltage. Thus, we extracted the rising time constant (τ_r) using the following equation, $I_{\text{rising}}(t) = I_0 + I_g(1 - \mathrm{e}^{-(t-t_0)/\tau_r})$, where I_{rising} is the current as a function of time during the rising phase under UV illumination, I_0 is the base current, I_g is the current generation constant, and t is the time after UV illumination begins, t_0 is the UV illumination starting time. As shown in Fig. 3(c), the rising time constant showed a clear decreasing trend with the applied voltage, which supports the intrinsic QW structures. Here, we assumed that the following three factors are the most dominant mechanisms for the PPC considering the energy structure of the intrinsic QWs: (1) trap-mediated recombination; (2) recombination after de-trapping from the QW; and (3) escape from the QW and transport to the electrode. We extracted three decay time constants by using the following equation, $I_{\text{decay}}(t) = I_0 + I_1\mathrm{e}^{-(t-t_0)/\tau_1} + I_2\mathrm{e}^{-(t-t_0)/\tau_2} + I_3\mathrm{e}^{-(t-t_0)/\tau_3}$, where I_{decay} is the decay current after UV illumination, I_1, I_2, and I_3 are the current contacts for each component; and τ_1, τ_2, and τ_3 are the decay time constants for each component. Assuming that the trap-mediated recombination is more rapid than the QW-mediated recombination because of their energy level difference and the high vertical electric field, τ_1, τ_2, and τ_3 would attribute to the

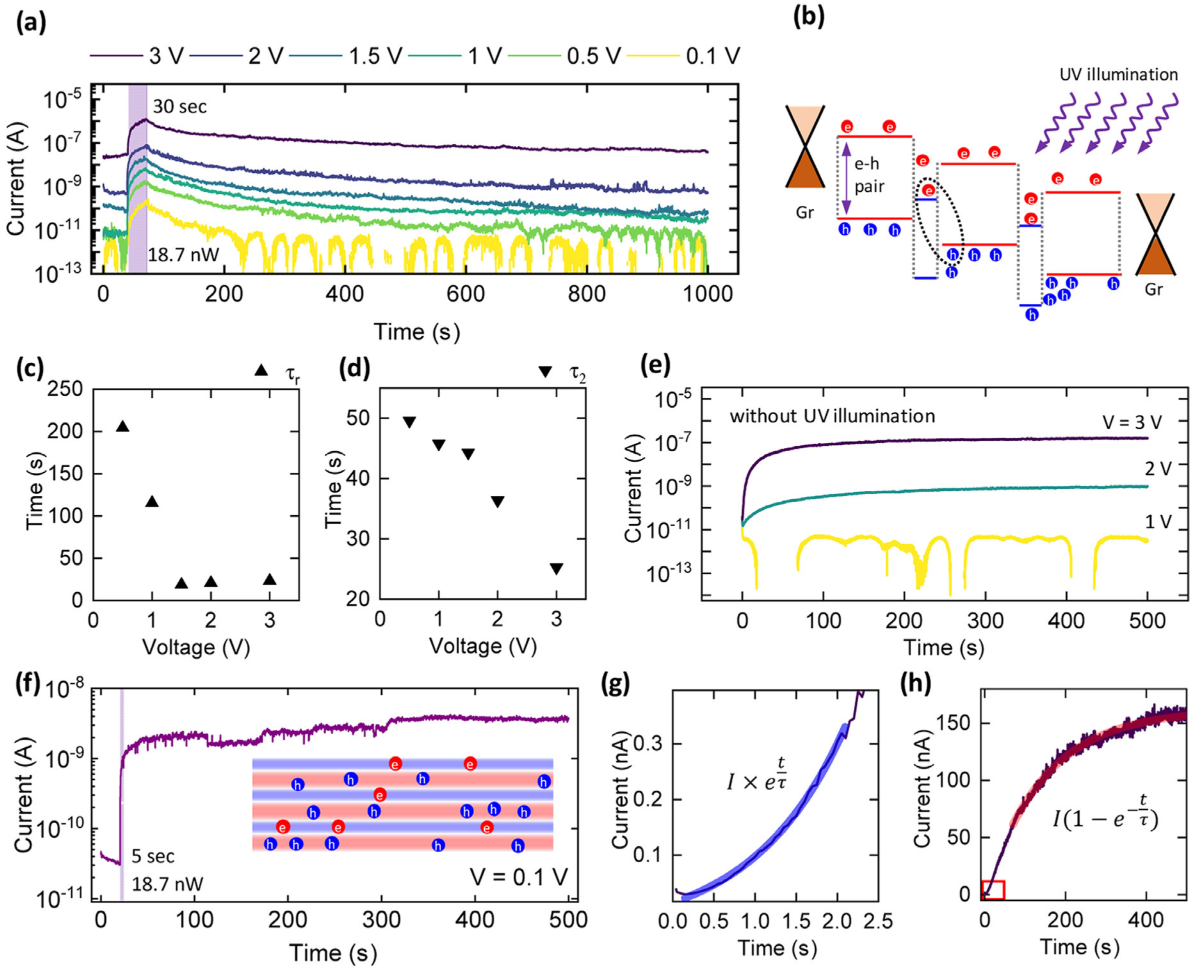

Fig. 3. (a) PPC characteristics of the vertical junction device with different applied voltages. (b) Energy band schematic of the vertical junction device under UV illumination. (c) Extracted τ_r and (d) τ_2 values at different applied voltages. (e) Anomalous charging behaviors of the lateral HSNO device without light illumination and upon varying applied voltage from 1 to 3 V. (f) Charging characteristic with UV illumination. The voltage was fixed at 0.1 V and the device was UV-illuminated for 5 s. Charging characteristics at the (g) very early stage and (h) later stage.

decay time constant of the trap-mediated recombination, QW-mediated recombination, and escape from the QW, respectively. Therefore, the decay time constant of the QW-mediated recombination is assumed to be inversely dependent on the applied voltage across the vertical junction since the trapped charges, which contributed to the PPC would be more rapidly extracted out as the applied voltage increased (Fig. S30). Therefore, τ_2 decreases as the applied voltage increases, as shown in Fig. 3(d).

Moreover, the injected charges from the electrodes could show a behavior identical to the photogate effect, because any charge, not only photogenerated excitons, will be trapped in the QWs, resulting in enhanced conductivity. To verify this, the lateral structured devices with the HSNO flakes of approximately 10 nm thickness, similar to vertical-structured devices, were fabricated to maximize the effects of QWs, e.g., charge trapping behavior. Due to the longer channel length compared to vertical one, more charge carriers can be trapped along the channel. This longer channel length leads to more significant changes in current, affecting the charge transport characteristics. In the lateral configuration, the electric field is typically lower compared to the vertical configuration, which also influences the charge trapping. Surprisingly, the channel conductivity was gradually enhanced by four orders of magnitude for a few hundreds of seconds by applying 3 V across the lateral channel (V_{lateral}) without any illumination, as shown in Fig. 3(e). This result originated from the aforementioned charge trapping into the QWs. Specifically, the conductivity did not change at V_{lateral} of 1 V showing insulating behaviour which indicates that the injected charges cannot overcome the energy barriers of QWs; thus, they cannot contribute to the conductivity enhancement. However, when the high-energy UV illumination would assist in the generation of trapped charges, even a small V_{lateral} of 0.1 V could contribute to the enhanced conductivity as shown in Fig. 3(f). In particular, the enhanced current level did not decrease for a few hundred seconds; rather, it increased. As a result, we could not even extract the decay time constant. At the very early stage, we assumed that all injected charges will be trapped in the QW, increasing the conductance. Therefore, the current should increase exponentially as follows: $I_{\text{initial}}(t) \propto I_0 e^{\frac{t}{\tau}}$, where I_{initial} is the current at the onset of the charge trapping process. As shown in Fig. 3(g), the early stage of the charging curves was well-fitted with our model, and the charging behaviour would follow the field-charging equation where there are a limited number of QWs and corresponding energy states with a constant voltage bias, $I_{\text{charging}}(t) = I_0(1 - e^{-t/\tau})$ where I_{charging} is the current during the charge trapping process, in which trapped charges progressively hinder further charging (Fig. 3(h)). The later stage of the charging behavior also followed the fitting curve well. As expected, the extracted charging time constant under the 3 V condition (~147.3 s) was found to be much smaller than that under the 2 V condition (~281.8 s), indicating that more charges are injected and trapped

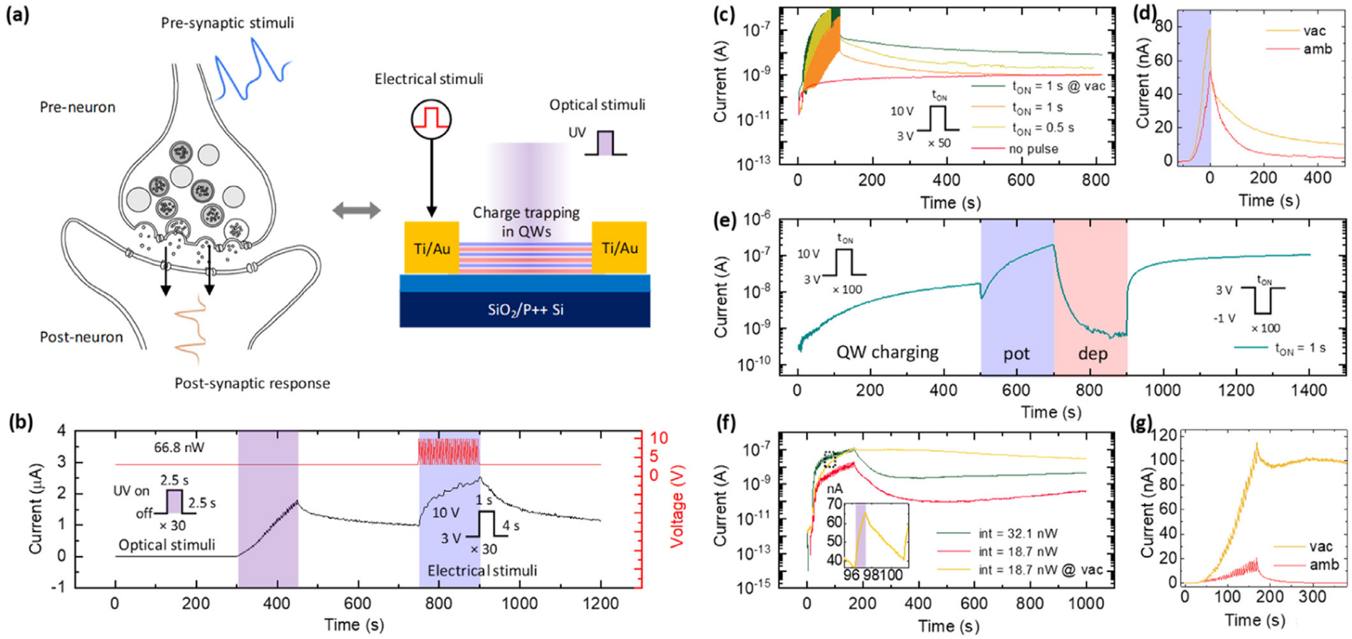

Fig. 4. (a) Schematic of biological neurons and artificial synaptic device. (b) Artificial synaptic behavior of the lateral HSNO device with optical and electrical stimuli. (c) Logarithmic and (d) linear artificial synaptic characteristics of the lateral HSNO device with electrical stimuli under various measurement conditions. (e) Potentiation and depression of the device. (f) Logarithmic and (g) linear artificial synaptic characteristics of the lateral HSNO device with UV stimuli under abmient and vacuum conditions.

in the intrinsic ionic layered structures for the same time period under the higher voltage condition. We would like to note that we did not observe a noticeable difference in the charging effect between devices with different SNO thicknesses, except for the monolayer device, as monolayer SNO cannot have a QW structure. We assume this is because the number of QWs increases with thickness, maintaining the volumetric portion of QW structures and thereby limiting the charge trapping concentration.

2.3. Proof-of-concept for artificial synaptic devices

Given that the intrinsic highly-ordered QW structure shows unprecedented PPC and conductivity enhancement, we demonstrated a proof of concept for artificial synaptic devices with HSNO flakes by exploiting the charge trapping nature of QWs as illustrated in Fig. 4(a) [16–27]. Taking advantage of the tenable enhanced conductivity of HSNO due to its charging behaviors in the ionic layered structure, we successfully demonstrated artificial synaptic devices that can be simultaneously controlled by both UV spikes and voltage pulses, as shown in Fig. 4(b). The structures of optical and electrical stimuli are presented in detail in the Supplementary materials and the read voltage was fixed at 3 V, while the current measurement. The conductivity increased around 10^3 times after the UV spikes were applied (see the Supplementary materials Section 6), exhibiting a highly linear potentiation, as shown in Fig. 4(b). After a few hundred seconds, the artificial synaptic device was again potentiated with voltage spikes. In our ionic layered system, such synaptic behaviors arise from the charging nature of the QWs regardless of whether the trapped charges in the QW are injected by applied voltage or generated by UV illumination, leading to both optical and electrical potentiation. We also verified that the potentiation could be tuned by modulating not only the time and amplitude of the stimulation, as shown in Fig. 4(c), but also the surrounding environmental conditions (the Supplementary materials Section 9). As shown in Fig. 4(d), a higher and longer conductivity enhancement (i.e. potentiation) was observed in vacuum because the trapped charges could not be donated or withdrawn by oxygen and water molecules at the surface of the HSNO flakes, but trapped in the QWs. Specifically, by increasing the tunneling probability, we were able to reduce both energy consumption and the duration of the voltage pulse, presenting an opportunity for further improvement. Such an adjustment facilitated a comparable change in conductivity due to a similar quantity of charges trapped in the QWs (Fig. S35). The depression behaviors have been also demonstrated, since the charges that are trapped by the physically outer QWs or shallowly trapped can be again extracted by applying a negative voltage pulse, whereas the charges in deeper wells are difficult to be de-trapped (Fig. 4(e)). The conductivity slowly increased as soon as 3 V of read voltage was applied due to charging and increased rapidly under positive voltage pulses. Sequentially, the negative voltage pulse made the device depressed by taking out trapped charges from shallow levels and/or outer QWs, leading to the suppression of conductivity. As soon as the depression sequence ended, the conductivity rapidly recovered within a few tens of seconds. In a lateral HSNO device, QWs are sequentially connected along the channel, and the QWs are filled and emptied from the electrode where charges are injected or withdrawn. If we apply a small depression stimulus that is not strong enough to remove all the trapped charges from the QWs, there may be remaining trapped charges in the inner QWs or in some QWs with larger energy barriers. These remaining charges can accelerate charge injection by reducing potential barriers in the channel, leading to a rapid recovery of conductance. Such remaining charges can be sufficiently removed when we apply a larger depression voltage (Fig. S36). The potentiation by the optical spikes showed a behavior similar to the environmental effect. As the UV illumination power increased, the conductivity increased to a higher level, as shown in Fig. 4(f). Interestingly, the decay time was longer in vacuum than that under the ambient condition. In addition, it showed better linearity with the light stimuli, which indicates that excitons can be generated uniformly regardless of the spatial distribution of QWs. This can also support the longer decay time in vacuum than that under the ambient condition. Likewise, ionic 2D layered system can be a viable option for future neuromorphic devices due to their well-defined QWs. This is because ionic layered system does not require any structural

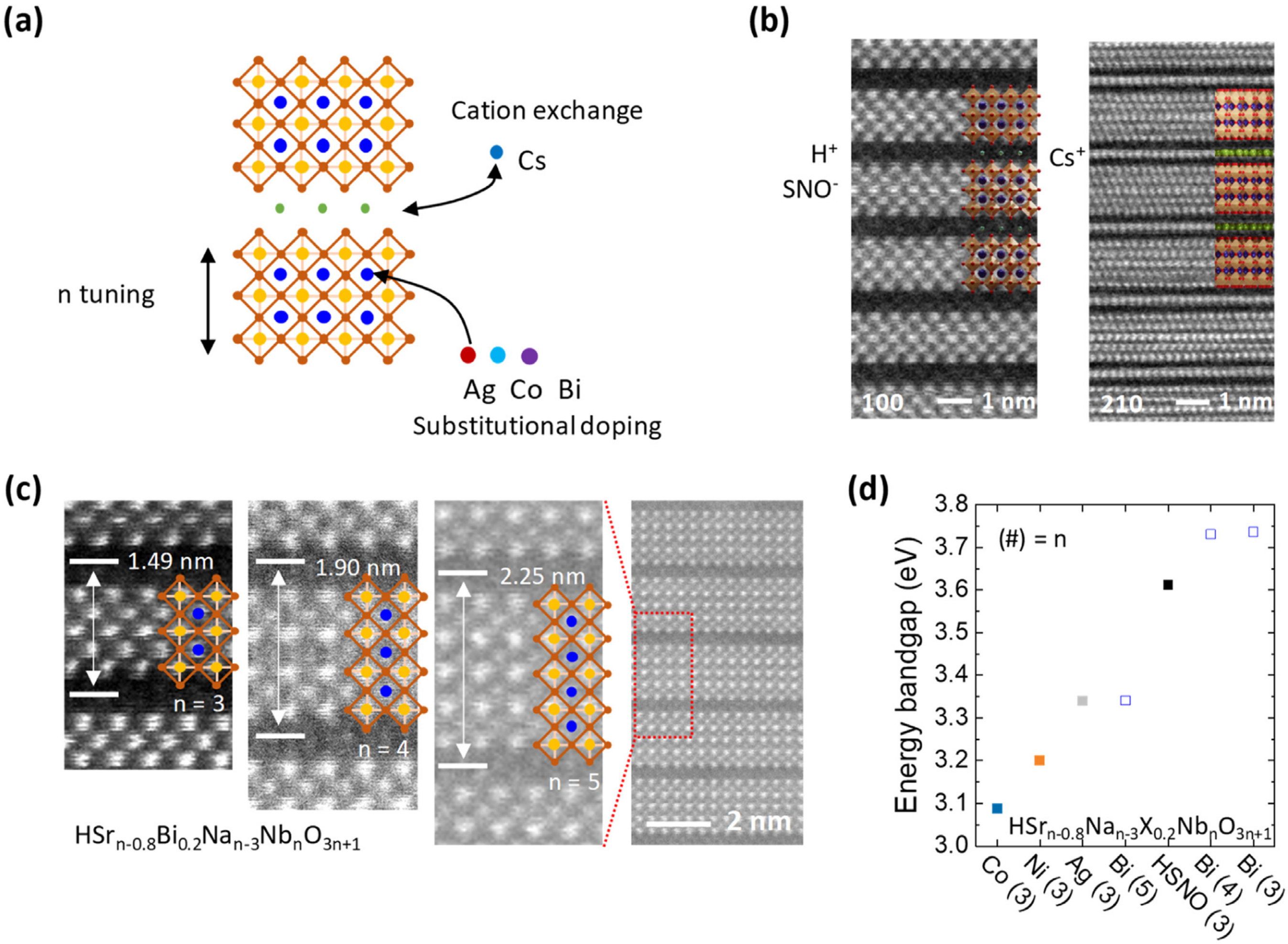

Fig. 5. (a) Schematic illustration of the high tunability of HSNO nanosheets through cation exchange and substitutional doping. (b) STEM images of HSNO (left) and CsSNO (right). (c) STEM images of Bi-doped SNO flakes with different composition rate numbers. (d) Energy bandgap energy of pristine SNO and doped-SNO flakes.

disorders or additional charge trapping layers to achieve resistance changes necessary for neuromorphic behaviour. The tunnelling and charge trapping in quantum wells provide the possibility of improved stability and the potential for reduced energy consumption and pulse width through increasing tunnelling probability.

2.4. High tunability of 2D oxide perovskite nanosheets

The intrinsic ionic layered system in 2D layered DJ-phase oxide perovskites also showed high tunability of material properties. Both the cation and anion layers can be substituted, introducing additional functionalities while the intrinsic ionic layered structure is well-maintained, as well as the quantum well spacing can be tailored as shown in Fig. 5(a). As a representative result of their cation tenability, the Cs^+ layers were substituted shown in the bottom STEM image of Fig. 5(b), maintaining the highly-ordered ionic layered structures with clean interfaces. These results support that the components of ionic layers can be variable upon demands. Furthermore, the number of perovskite layers (n) can be tailored without compromising the highly-ordered intrinsic ionic layered structure, in principle, n can be infinitely increased [42–44]. As shown in Fig. 5(c), as n was changed from 3 to 4 and 5, the spacing was increased, indicating the intrinsic quantum well spacing could also be changed. We extracted the energy bandgap of HSNO as a function of the different number of layers by conducting UV–Vis analysis. As expected, the bandgap significantly decreased as n increased owing to the quantum confinement effect, which also supports that 2D DJ-phase oxide perovskites having highly-ordered ionic layered structures have high tunability for various applications (Fig. 5(d)). The charge trapping behaviors could also be dependent on the composition and structure of 2D DJ-phase oxide perovskites which needed to be further explored through follow-up studies.

3. Conclusions

Unlike traditional 2D materials where charge trapping occurs due to disordered structures, HSNO nanosheets exhibit giant charge trapping behavior within their intrinsic and well-defined QW structures. This intrinsic charge trapping leads to significant enhancements in both electric and photoconductivity, highlighting the superiority of DJ-phase perovskites for innovative electronic and optoelectronic applications. The intrinsic layered ionic QW structures could be investigated in both vertical and lateral structured devices, owing to their compatibility with the vdW transfer technique and resultant atomically clean interfaces in the intrinsic QWs. Our findings allowed us to demonstrate the potential of artificial synaptic devices for electronic applications. Furthermore, cation or anion layers could be tuned while maintaining the favorable properties of the ionic layered structures. The energy bandgap could also be widely tailored depending on the composition number and dopants. To date, achieving atomically clean interfaces remains a formidable obstacle even for state-of-the-art methods in fabricating functional 2D heterostructures. Here, our intrinsically highly-ordered ionic layered system, even in a single 2D flake, has atomically clean interfaces and unique quantum mechanical properties, high tunability, stability, and processability offering huge opportunities as a novel 2D layered material platform.

4. Methods

4.1. Material preparation

All nanoflakes were produced using the solid-state synthesis method. We commenced by synthesizing parent materials, primarily containing K^+ ions in the perovskite layer, exemplified by KSNO. Subsequently, these K^+ ions were swapped with H^+ ions in an acidic medium. The resulting HSNO was then exfoliated to the desired thickness by substituting H^+ ions with TBA^+ ions which has a notably larger ionic radius and using centrifugation. To endow the nanoflakes with diverse properties, successful elemental substitutions were carried out at both the A-site and B-site of the HSNO. Furthermore, the number of perovskite layers within the nanoflakes was judiciously modulated through molecular thickness control. Experimental results underscored that both the size and thickness of the nanoflakes could be adeptly tailored by altering synthesis and centrifugation parameters. To showcase the potential for large-scale applications, we accomplished deposition of nanosheets on a 2-inch wafer utilizing the Langmuir–Blodgett (LB) method. Additionally, we have effectively realized thin film fabrication via inkjet printing. Comprehensive methodologies and results are elaborated in the Supplementary materials (Section 1).

4.2. Structural and chemical composition characterization

KSNO, HSNO, and SNO flakes were collected during the synthesis process to verify their crystallinity by X-ray diffraction (XRD, Dmax2500/PC, Rigaku) analysis. The chemical composition of the flakes were analysed using energy dispersive spectroscopy (EDS, Regulus 8230, Hitachi). The thickness of 2D materials was measured *via* AFM, NX10, Park Systems).

The intrinsic highly-ordered ionic layered structure was observed using HRTEM and STEM (TITAN 80–300, ThermoFisher Scientific). The samples for HRTEM and STEM were prepared by using the focused ion beam (FIB, Helios NanoLab 600, ThermoFisher Scientific) system.

The thermogravimetric analysis and differential scanning calorimetry (SDT Q600, TA instruments) were conducted by varying the temperature from 0 to 1500 °C.

Optical bandgaps of nanoflakes colloidal solution were evaluated from the Tauc plot by UV–visible NIR spectrophotometer (Cary 5000, Agilent) in the wavelength range of 200–1000 nm. The high concentrations of nanoflakes colloidal solution were diluted by DI water to avoid the noise and saturation of the detector.

The dielectric properties of SNO and Bi-doped SNO flakes were investigated with an impedance analyser (4294A, Agilent) as thin film form by Langmuir–Blodgett (LB) method. The SNO and SBNO colloidal solution was spread onto the DI water surface in LB trough and compressed by barriers until an appropriate surface pressure. Then, uniformly compressed flakes were transferred onto the P^{++} Si substrate repeatedly. Using a shadow mask, the Au top electrodes were deposited on the surface of nanoflakes thin films by a quick sputtering system.

The magnetisation hysteresis loops of Co, Fe, and Mn-doped SNO flakes were measured at room temperature using a vibrating sample magnetometer (FCM-10, Microsense) as a thin film formed by the electrophoretic deposition process. The thin films were deposited by applying a voltage difference of 50 V for 2 min between the P^{++} Si substrate (positive electrode, 1 cm × 1 cm) and a Pt counter electrode (negative electrode, 2 cm × 2 cm). After the deposition, the thin films were dried at 100 °C for 1 h in the air.

4.3. Device fabrication

The hemispherical PDMS stamps were prepared (SYLGARD 184). After the curing process at 120 °C for 1 h, the reactive ion etching (RIE, VITA, Femto Science) process was conducted to form a thin layer of SiO_2 layer on PDMS stamps, followed by spin-coating of polypropylene carbonate. Graphene and h-BN flakes were exfoliated from their bulk crystals (HQ graphene) and transferred onto a different SiO_2/Si substrate. For the electrode, an electron-beam lithography system (JSM-6510, JEOL) was used. The double-layer resist method was employed to allow the formation of fine structures. Methyl methacrylate (9 % concentration in ethyl lactate, Microchem) as a buffer layer and poly(methyl methacrylate) (PMMA 950k A5, Microchem) as an e-beam resist were sequentially deposited. After the development step, Ti/Au (3 nm/50 nm) were deposited using an electron-beam evaporator (KVE-E2004L, Korea Vacuum Tech.)

The lateral devices were fabricated in a similar way. After selecting a few layers of HSNO flakes, the patterns of electrodes were defined, and then Ti/Au (3 nm/50 nm) were deposited by using e-beam lithography and e-beam deposition, respectively.

4.4. Device characterizations

The electrical characterizations were conducted in a temperature variable probe station (M6VC, MS-Tech) with a semiconductor parameter analyzer (B1500A, Keysight, and SCS-4200, Keithley) under the vacuum condition at room temperature.

The optoelectronic properties of HSNO devices were measured in the probe station with the semiconductor parameter analyser in the sampling mode. The UV light was illuminated through the optical window by using a UV lamp (LGA0330F, Liim Tech.), varying the illumination power. The UV power was measured under the same condition by using a light power meter (PM160T, Thorlabs). The measured power values were converted, considering the device size and the sensor size of the power meter.

Data availability

The data that support the plots within this paper and other findings of this study are available from the corresponding authors upon reasonable request.

Declaration of competing interest

The authors declare that they have no known competing financial interests or personal relationships that could have appeared to influence the work reported in this paper.

CRediT authorship contribution statement

Kyungjune Cho: Writing – original draft, Validation, Investigation, Data curation, Conceptualization. **Haena Yim:** Writing – original draft, Methodology, Investigation, Formal analysis, Data curation, Conceptualization. **Gahui Park:** Validation, Formal analysis, Data curation. **Jiwoo Yang:** Validation, Formal analysis, Data curation. **So-Yeon Yoo:** Formal analysis, Data curation. **Jongwoo Nam:** Visualization, Validation, Investigation. **Minwoo Song:** Visualization, Validation. **Deok-Hwang Kwon:** Visualization, Validation. **Keehoon Kang:** Validation. **Takhee Lee:** Validation, Supervision. **Ji-Won Choi:** Writing – original draft, Supervision, Investigation. **Seungjun Chung:** Writing – review & editing, Writing – original draft, Visualization, Validation, Supervision, Data curation, Conceptualization.

Acknowledgements

This work was financially supported by the National Research Foundation of Korea (NRF) grant funded by the government of the Republic of Korea (the Ministry of Science and ICT) (Nos. NRF-2023R1A2C2003247, 2021R1C1C2091728, and 2021R1A2C2010695), the Nano & Material Technology Development Program through the National Research Foundation of Korea (NRF) funded by Ministry of Science and ICT (No. RS-2024–00402972), and the National Research Council of Science & Technology (NST) grant by the Korea government (MSIT) (No. CRC22031–000).

Supplementary materials

Supplementary material associated with this article can be found, in the online version, at doi:10.1016/j.jmst.2025.01.042.

References

[1] K.S. Novoselov, A. Mishchenko, A. Carvalho, A.H. Castro Neto, Science 353 (2016) aac9439.
[2] L. Du, T. Hasan, A. Castellanos-Gomez, G.-B. Liu, Y. Yao, C.N. Lau, Z. Sun, Nat. Rev. Phys. 3 (2021) 193–206.
[3] M. Gibertini, M. Koperski, A.F. Morpurgo, K.S. Novoselov, Nat. Nanotechnol. 14 (2019) 408–419.
[4] A. Ciarrocchi, F. Tagarelli, A. Avsar, A. Kis, Nat. Rev. Mater. 7 (2022) 449–464.
[5] W. Huh, D. Lee, C.-H. Lee, Adv. Mater. 32 (2020) 2002092.
[6] Z. Lin, Y. Huang, X. Duan, Nat. Electron. 2 (2019) 378–388.
[7] A.K. Geim, I.V. Grigorieva, Nature 499 (2013) 419–425.
[8] Y. Liu, N.O. Weiss, X. Duan, H.-C. Cheng, Y. Huang, X. Duan, Nat. Rev. Mater. 1 (2016) 1–17.
[9] F.-S. Yang, M. Li, M.-P. Lee, I.-Y. Ho, J.-Y. Chen, H. Ling, Y. Li, J.-K. Chang, S.-H. Yang, Y.-M. Chang, K.-C. Lee, Y.-C. Chou, C.-H. Ho, W. Li, C.-H. Lien, Y.-F. Lin, Nat. Commun. 11 (2020) 2972.
[10] F.-S. Yang, M. Li, M.-P. Lee, I.-Y. Ho, J.-Y. Chen, H. Ling, Y. Li, J.-K. Chang, S.-H. Yang, Y.-M. Chang, K.-C. Lee, Y.-C. Chou, C.-H. Ho, W. Li, C.-H. Lien, Y.-F. Lin, Nanoscale 13 (2021) 16156–16163.
[11] K. Cho, T.-Y. Kim, W. Park, J. Park, D. Kim, J. Jang, H. Jeong, S. Hong, T. Lee, Nanotechnology 25 (2014) 155201.
[12] T.-H. Tsai, Z.-Y. Liang, Y.-C. Lin, C.-C. Wang, K.-I. Lin, K. Suenaga, P.-W. Chiu, ACS Nano 14 (2020) 4559–4566.
[13] I. Amit, T.J. Octon, N.J. Townsend, F. Reale, C.D. Wright, C. Mattevi, M.F. Craciun, S. Russo, Adv. Mater. 29 (2017) 1605598.
[14] Q. Zhao, W. Wang, F. Carrascoso-Plana, W. Jie, T. Wang, A. Castellanos-Gomez, R. Frisenda, Mater. Horiz. 7 (2020) 252–262.
[15] J. Chen, M.-Y. Sun, Z.-H. Wang, Z. Zhang, K. Zhang, S. Wang, Y. Zhang, X. Wu, T.-L. Ren, H. Liu, L. Han, Nano-Micro Lett. 16 (2024) 264.
[16] J.J. Yang, D.B. Strukov, D.R. Stewart, Nat. Nanotechnol. 8 (2013) 13–24.
[17] H. Ma, H. Fang, X. Xie, Y. Liu, H. Tian, Y. Chai, Nano-Micro Lett. 16 (2024) 104.
[18] V.K. Sangwan, M.C. Hersam, Nat. Nanotechnol. 15 (2020) 517–528.
[19] D. Ielmini, H.-S.P. Wong, Nat. Electron. 1 (2018) 333–343.
[20] G. Cao, P. Meng, J. Chen, H. Liu, R. Bian, C. Zhu, F. Liu, Z. Liu, Adv. Funct. Mater. 31 (2021) 2005443.
[21] Y. Shi, X. Liang, B. Yuan, V. Chen, H. Li, F. Hui, Z. Yu, F. Yuan, E. Pop, H.-S.P. Wong, M. Lanza, Nat. Electron. 1 (2018) 458–465.
[22] R. Ge, X. Wu, M. Kim, J. Shi, S. Sonde, L. Tao, Y. Zhang, J.C. Lee, D. Akinwande, Nano Lett. 18 (2018) 434–441.
[23] K.C. Kwon, J.H. Baek, K. Hong, S. Kim, H. Jang, Nano-Micro Lett. 14 (2022) 58.
[24] S. Kumar, X. Wang, J.P. Strachan, Y. Yang, W.D. Lu, Nat. Rev. Mater. 7 (2022) 575–591.
[25] J. Chen, X. Liu, Q. Zhu, X. Fang, W. Xu, Adv. Funct. Mater. 34 (2024) 2402684.
[26] F. Cao, E. Hong, Z. Hu, Y. Liu, B. Sun, J.-H. He, X. Fang, Nano Energy 120 (2024) 109135.
[27] Z. Xi, M. Liu, J.-H. Zhang, S. Zhang, L. Li, S. Li, M. Jiang, W. Tang, Z. Liu, Adv. Opt. Mater. 12 (2024) 2402193.
[28] A.G. Ricciardulli, S. Yang, J.H. Smet, M. Saliba, Nat. Mater. 20 (2021) 1325–1336.
[29] A.J. Yang, K. Han, K. Huang, C. Ye, W. Wen, R. Zhu, R. Zhu, J. Xu, T. Yu, P. Gao, Q. Xiong, X.R. Wang, Nat. Electron. 5 (2022) 233–240.
[30] S. Li, Y. Zhang, W. Yang, H. Liu, X. Fang, Adv. Mater. 32 (2020) 1905443.
[31] Y. Zhang, S. Li, Z. Li, H. Liu, X. Liu, J. Chen, X. Fang, Nano Lett. 21 (2021) 382–388.
[32] M. Liu, T. Pauporté, Nano-Micro Lett. 15 (2023) 134.
[33] W. Sirisaksoontorn, A.A. Adenuga, V.T. Remcho, M.M. Lerner, J. Am. Chem. Soc. 133 (2011) 12436–12438.
[34] P.M. Campbell, A. Tarasov, C.A. Joiner, W.J. Ready, E.M. Vogel, ACS Nano 9 (2015) 5000–5008.
[35] K. Kinoshita, R. Moriya, S. Okazaki, Y. Zhang, S. Masubuchi, K. Watanabe, T. Taniguchi, T. Sasagawa, T. Machida, Nano Lett. 22 (2022) 4640–4645.
[36] K. Takeyama, R. Moriya, S. Okazaki, Y. Zhang, S. Masubuchi, K. Watanabe, T. Taniguchi, T. Sasagawa, T. Machida, Nano Lett. 21 (2021) 3929–3934.
[37] K. Czerniak-Łosiewicz, A.P. Gertych, M. Świniarski, J. Judek, M. Zdrojek, J. Phys. Chem. C 124 (2020) 18741–18746.
[38] C. Jin, E.Y. Ma, O. Karni, E.C. Regan, F. Wang, T.F. Heinz, Nat. Nanotechnol. 13 (2018) 994–1003.
[39] W.J. Yu, Q.A. Vu, H. Oh, H.G. Nam, H. Zhou, S. Cha, J.-Y. Kim, A. Carvalho, M. Jeong, H. Choi, A.H. Castro Neto, Y.H. Lee, X. Duan, Nat. Commun. 7 (2016) 13278.
[40] T.C.L.G. Sollner, H.Q. Le, C.A. Correa, W.D. Goodhue, Appl. Phys. Lett. 47 (1985) 36.
[41] T.T. Chen, W.S. Su, Y.F. Chen, Appl. Phys. Lett. 85 (2004) 1526.
[42] V. Thangadurai, P. Schmid-Beurmann, W. Weppner, J. Solid State Chem. 158 (2001) 279–289.
[43] L. Mao, R.M. Kennard, B. Traore, W. Ke, C. Katan, J. Even, M.L. Chabinyc, C.C. Stoumpos, M.G. Kanatzidis, Chem 5 (2019) 2593–2604.
[44] J.K. Harada, N. Charles, K.R. Poeppelmeier, J.M. Rondinelli, Adv. Mater. 31 (2019) 1805295.